

Crystal structure of CaRhO₃ polymorph: High-pressure intermediate phase between perovskite and post-perovskite

Y. SHIRAKO,¹ H. KOJITANI,¹ A.R. OGANOV,^{2,3} K. FUJINO,⁴ H. MIURA,⁵ D. MORI,¹ Y. INAGUMA,¹ K. YAMAURA,⁶ AND M. AKAOGI^{1,*}

¹Department of Chemistry, Gakushuin University, Toshima-ku, Tokyo 171-8588, Japan

²Department of Geosciences and Department of Physics and Astronomy, Stony Brook University, Stony Brook, New York 11794-2100, U.S.A.

³Geology Department, Moscow State University, 119992 Moscow, Russia

⁴Geodynamics Research Center, Ehime University, Bunkyo-cho, Matsuyama 790-8577, Japan

⁵Division of Earth and Planetary Sciences, Hokkaido University, Kita-ku, Sapporo 060-0810, Japan

⁶National Institute of Materials Science, Namiki, Tsukuba 305-0044, Japan

ABSTRACT

A high-pressure phase of CaRhO₃ stable between perovskite and post-perovskite in *P-T* space was synthesized at 17 GPa and 1650 °C using a multi-anvil apparatus. The crystal structure of CaRhO₃ was solved by the structure prediction evolutionary algorithm and was refined by Rietveld analysis of the synchrotron powder X-ray diffraction pattern, along with transmission electron microscopy observations. The structure is monoclinic with lattice parameters of $a = 12.5114(1) \text{ \AA}$, $b = 3.1241(1) \text{ \AA}$, $c = 8.8579(1) \text{ \AA}$, $\beta = 103.951(1)^\circ$, $V = 336.01(1) \text{ \AA}^3$ with space group $P2_1/m$. The structure contains edge-sharing RhO₆ octahedral chains along the *b*-axis. The six RhO₆ octahedral chains make a unit, which stacks up alternatively with the CaO₈ polyhedral layer along the [101] direction to form the structure of CaRhO₃ intermediate phase.

Keywords: Perovskite, post-perovskite, X-ray diffraction, Rietveld analysis, CaRhO₃, electron microscopy, structure search

INTRODUCTION

Since magnesium-rich silicate perovskite, the predominant mineral in the Earth's lower mantle, was found to transform to a CaIrO₃-type post-perovskite phase at pressure-temperature conditions of the lowermost mantle (Murakami et al. 2004; Oganov and Ono 2004), several experimental and theoretical studies on post-perovskite have been performed from viewpoints of mineral physics and geophysics. Analog materials that exhibit a transition to the post-perovskite phase at pressure lower than magnesium silicate are of significant interest to obtain insights to the properties of magnesium silicate post-perovskite, particularly for the analog post-perovskite phases quenchable to ambient conditions. CaIrO₃ perovskite transforms to post-perovskite at around 2 GPa (Hirose and Fujita 2005; Kojitani et al. 2007a), and CaRuO₃ perovskite also shows the same transition at about 20 GPa (Kojitani et al. 2007b). Both CaPtO₃ and CaRhO₃ crystallize into the post-perovskite structure at around 5 GPa (Ohgushi et al. 2008; Inaguma et al. 2008; Shirako et al. 2009). Recently, it was reported that CaSnO₃ perovskite transforms to post-perovskite at about 40 GPa (Tateno et al. 2010). These post-perovskite phases of CaMO₃ ($M = \text{Ir, Ru, Rh, Pt, and Sn}$) are quenchable to ambient conditions. In addition to the interest in Earth science, the post-perovskite oxides are of significant interest in materials science because of characteristic physical properties based on the quasi-two-dimensional lattice (Ohgushi et al. 2006; Yamaura et al. 2009; Shirako et al. 2010, 2011; Cheng et al. 2011; Hirai et al. 2011).

In our high-pressure transition study of CaRhO₃ perovskite,

we found that an intermediate phase with an unknown structure is stable between perovskite and post-perovskite at around 5–20 GPa above ~1200 °C (Shirako et al. 2009). The intermediate phase was observed to have a monoclinic symmetry and its molar volume was noted to be 1.1% smaller than that of perovskite and 0.7% greater than that of post-perovskite. To our knowledge, CaRhO₃ is the first material that has a phase stable between perovskite and post-perovskite. Oganov et al. (2005) theoretically proposed a new type of kinked post-perovskite structures that are intermediate between perovskite and post-perovskite, and serve as intermediate states for the phase transition from perovskite to post-perovskite. Tschauner et al.'s (2008) experimental and theoretical studies suggest that aluminous magnesium silicate post-perovskite could have a similar kinked post-perovskite structure, instead of the CaIrO₃-type post-perovskite structure. Yamanaka et al. (2010) concluded that the space group of iron-rich (Mg,Fe)SiO₃ post-perovskite is not *Cmcm* of CaIrO₃-type, but *Pmma*. Therefore, the structure of CaRhO₃ intermediate phase is of special interest from a viewpoint of crystal-chemical relationship with perovskite and post-perovskite. In this study, we have analyzed the structure through a theoretical search of the model structure and the structure refinement with Rietveld analysis of powder X-ray diffraction (XRD) data, along with transmission electron microscopy (TEM) observations.

EXPERIMENTAL AND THEORETICAL METHODS

Sample synthesis

CaRhO₃ perovskite was used as the starting material of the intermediate phase. The perovskite phase was synthesized at the National Institute of Materials Science in a similar manner to that carried out by Yamaura and Takayama-Muromachi

* E-mail: masaki.akaogi@gakushuin.ac.jp

(2006). The mixture of CaO, Rh₂O₃, and KClO₄ (molar ratio of 2:1:0.265) was packed into an MgO capsule, which was enclosed in a platinum capsule. The double capsule was placed in the central part of the pyrophyllite pressure medium. KClO₄ was added to oxidize Rh³⁺ to Rh⁴⁺. The inner MgO capsule was used to prevent the sample powder from reacting with the Pt capsule. The sample was pressurized to 6 GPa and heated at 1900 °C for 30 min, and then annealed at 1600 °C for 30 min by a belt-type high-pressure apparatus. The sample surface in contact with the MgO capsule was removed, and KCl synthesized in the sample was washed out in water. After the treatments, the synthesized powder of CaRhO₃ perovskite was examined by powder XRD to confirm to be the single phase material. Compositional analysis confirmed that the Ca:Rh atomic ratio was 1:1 in the synthesized sample. The CaRhO₃ intermediate phase was synthesized using a Kawai-type 6-8 multi-anvil apparatus at Gakushuin University. Tungsten carbide anvils were used as the second-stage anvils. A semi-sintered MgO octahedron and a cylindrical Pt heater were used as the pressure medium and the heating element, respectively. For thermal insulation, a LaCrO₃ sleeve was put outside of the Pt heater together with two LaCrO₃ end-plugs. The CaRhO₃ perovskite synthesized earlier was packed into a tubular platinum capsule with KClO₄ in a molar ratio of 8:1. KClO₄ powder was added to prevent Rh⁴⁺ from reducing to Rh³⁺. A BN sleeve and lids were inserted between the platinum capsule and heater for electrical insulation. Temperature was measured by a Pt-Pt/13%Rh thermocouple, the hot junction of which was positioned at the central part of the Pt heater. The sample was held at 17 GPa and 1650 °C for 30 min, then quenched to room temperature under pressure, and was decompressed slowly to ambient pressure. KCl in the recovered sample was removed by washing in water. The sintered sample of the intermediate phase of about 15 mg was obtained. The synthesized sample was examined by micro-focus and powder XRD apparatus (CrK α radiation), indicating that the sample was the intermediate phase, along with a small amount of RhO₂ phase. Analysis by a scanning electron microscope with an energy-dispersive X-ray spectrometer (SEM-EDX) confirmed that the Ca:Rh ratio of the intermediate phase was the same as that of CaRhO₃ perovskite, and that a small amount of the RhO₂ phase was present in the run product. The SEM observation indicated that the crystal morphology of the intermediate phase was prismatic.

Synchrotron XRD experiments and TEM observations

Synchrotron powder XRD experiments were carried out at SPring-8 BL02-B2 beamline, where a Debye-Scherrer camera was used. The XRD data were obtained in a 2 θ range from 3 to 75° with an angle resolution of 0.01°. The X-ray wavelength was determined as 0.77462 Å from the XRD pattern of fluorite-type CeO₂ standard material. The synthesized CaRhO₃ intermediate phase, finely ground in an agate mortar, was packed in a glass capillary. The XRD data were collected by rotating the capillary. The XRD pattern of CaRhO₃ intermediate phase was analyzed by maximum-entropy method/Rietveld refinements using RIETAN-FP/VENUS package (Izumi and Momma 2007).

For TEM observations, a thin foil of CaRhO₃ intermediate phase was prepared by a Gatan ion-milling system Model 691 PIPS. A small chip (~0.2 mm) was taken from the central part of the sintered sample and Ar ion-milled with an accelerating voltage of 3.5 keV and a gun current of ~5 μ A. TEM observations of the foil were performed with a 200 kV JEOL JEM 2010 transmission electron microscope at the Geodynamics Research Center, Ehime University.

Theoretical structure searching

To find the structure, we employed the structure prediction evolutionary algorithm USPEX (Oganov and Glass 2006; Glass et al. 2006) with the fingerprint niching technique (Lyakhov et al. 2010). USPEX searches for the global minimum of free energy of the crystal with respect to its structural parameters. As no assumptions are made regarding the structure or its symmetry, this algorithm is capable of discovering completely unexpected or even hitherto unknown crystal structure types; see Oganov et al. (2006, 2009, 2010a, 2010b, 2011), Ma et al. (2009), and Gao et al. (2010) for reviews and select of applications of this methodology. While USPEX does not require any experimental information, incorporating such information (when it is available) in structure searches is beneficial; here we performed calculations using experimental unit-cell parameters with six formula units by Shirako et al. (2009). In these calculations, we used 40 structures in each generation, with 60% of the lowest-enthalpy structures allowed to produce the next generation through heredity (75%), and atomic permutation (15%); in addition, six distinct lowest-enthalpy structures were allowed to survive into the next generation. All the structures were fully relaxed and their energies were evaluated using density functional calculations within the generalized gradient approximation (Perdew et al. 1996) and employing the projector augmented wave (PAW) method (Bloechl

1994; Kresse and Joubert 1999), as implemented in the VASP code (Kresse and Furthmüller 1996). We used the [Ne] core PAW potential for Ca (outermost core radius of 2.3 a.u.), [Zn] core PAW potential for Rh (outermost core radius of 2.3 a.u.), and [He] core PAW potential for O (outermost core radius of 1.52 a.u.). Brillouin zone sampling was done by Monkhorst-Pack meshes of resolution $2\pi \times 0.1 \text{ \AA}^{-1}$ with finite temperature electronic smearing, and we used a plane wave basis set with the kinetic energy cutoff of 400 eV—these settings proved sufficient for obtaining precise energy differences between different structural rearrangements within the fixed unit cell. These calculations have produced the structural model, which was subsequently confirmed by our experimental crystal structure refinements.

RESULTS AND DISCUSSION

The TEM observations of six grains of several micrometers in diameter indicated the diffraction patterns consistent with the monoclinic cell of the lattice parameters determined by the powder XRD (Shirako et al. 2009). Figures 1a and 1b illustrate the electron diffraction patterns of $hk0$ and $h0l$ reciprocal lattice planes of the different grains, respectively. Apparently, there was no systematic absence of the spots including $0k0$. However, the spots of $0k0$ with $k = \text{odd}$ disappeared by declining the $hk0$ plane from the Bragg condition, showing the existence of 2_1 along the **b**-axis. This signifies that the possible space group of the intermediate phase is $P2_1$ or $P2_1/m$. The diffraction spots were sharp and showed a single-crystal pattern in most of the cases, but occasionally, they revealed a (100) or (101) twinned pattern with very weak diffuse streaks along the $[100]^*$ or $[101]^*$ direction, respectively. Also, the high-magnification transmission images showed very few stacking fault-like patterns parallel to (100) (Fig. 1c). From these TEM observations, the CaRhO₃ intermediate phase is considered to have a monoclinic $P2_1$ or $P2_1/m$ unit cell with almost no structure disorder.

The structure model of the lowest energy obtained by USPEX has a monoclinic unit cell with the space group $P2_1/m$. The space group is one of the two possible space groups suggested from the powder XRD data (Shirako et al. 2009) and the TEM observations shown above. The obtained atomic coordinates of the structure model were used as the initial values for the Rietveld analysis. Figure 2 shows the obtained synchrotron powder XRD pattern of CaRhO₃ intermediate phase. The XRD pattern was analyzed by Rietveld refinements, and the calculated XRD pattern is shown in Figure 2 to compare with the observed one. As the sample contained a small amount of the high-pressure polymorph of RhO₂ with the pyrite structure (Shirako et al., in preparation), it was included as the second phase in the Rietveld refinements. Site occupancies for all the atoms of CaRhO₃ intermediate phase were fixed to unity. Atomic displacement parameters (B) of oxygen were not refined, because they converged to negative values or unreasonably large positive ones. Therefore, they were fixed to be 1.0, similar to CaRhO₃ perovskite and post-perovskite (Shirako et al. 2009).

The refined structural parameters of CaRhO₃ intermediate phase are shown in Table 1. The reliability factor for the whole diffraction pattern, R_{wp} , was relatively small (6.2%), and those for whole reflections, R_B and R_F , for CaRhO₃ intermediate phase converged to less than 1%. The refined crystal structure of CaRhO₃ intermediate phase is reasonable as described below. The lattice parameters obtained by the Rietveld refinements are as follows: $a = 12.5114(1)$, $b = 3.1241(1)$, $c = 8.8579(1)$ Å, $\beta = 103.951(1)^\circ$, $V = 336.01(1)$ Å³, which are very close to those obtained by Shirako et al. (2009).

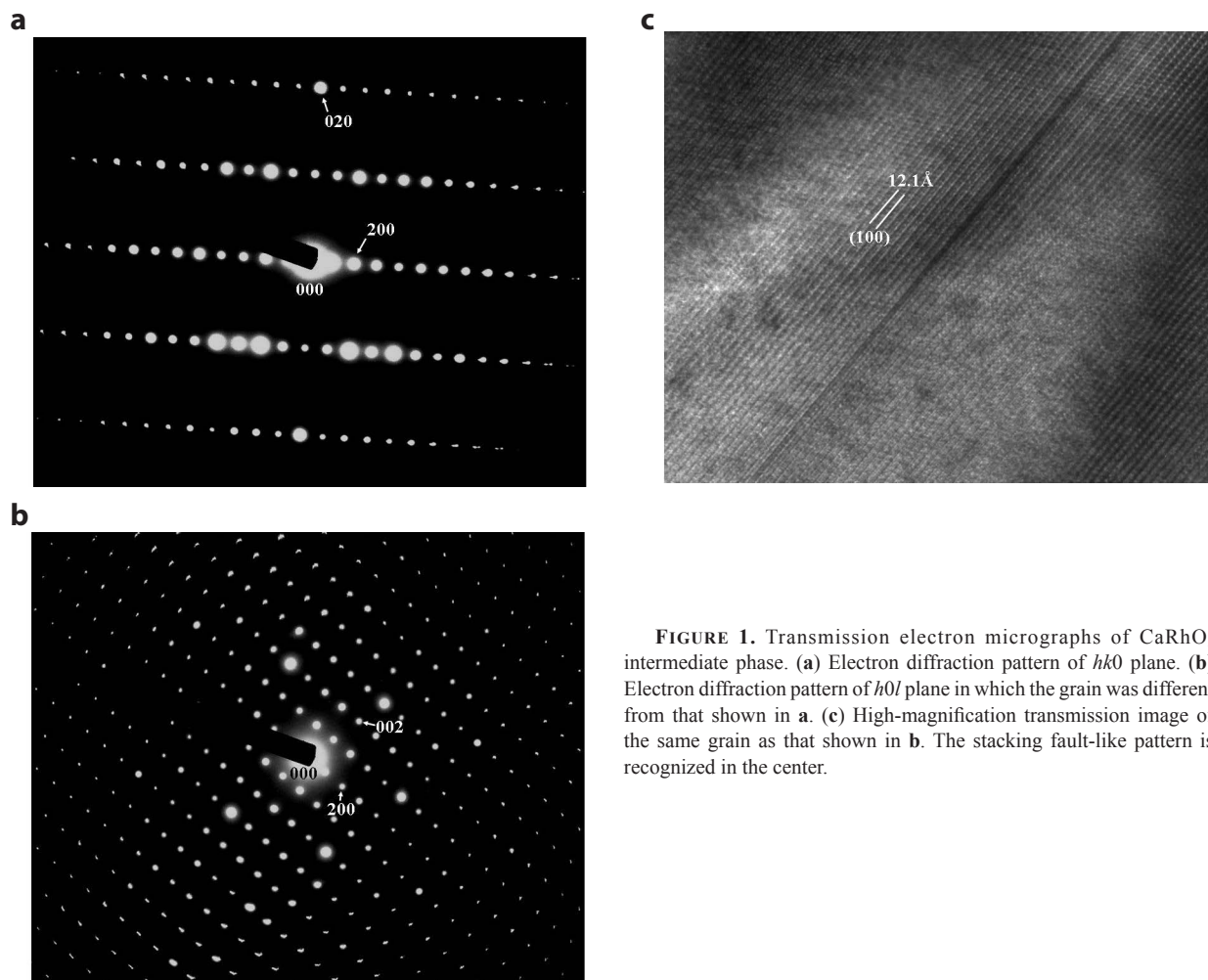


FIGURE 1. Transmission electron micrographs of CaRhO₃ intermediate phase. (a) Electron diffraction pattern of $hk0$ plane. (b) Electron diffraction pattern of $h0l$ plane in which the grain was different from that shown in a. (c) High-magnification transmission image of the same grain as that shown in b. The stacking fault-like pattern is recognized in the center.

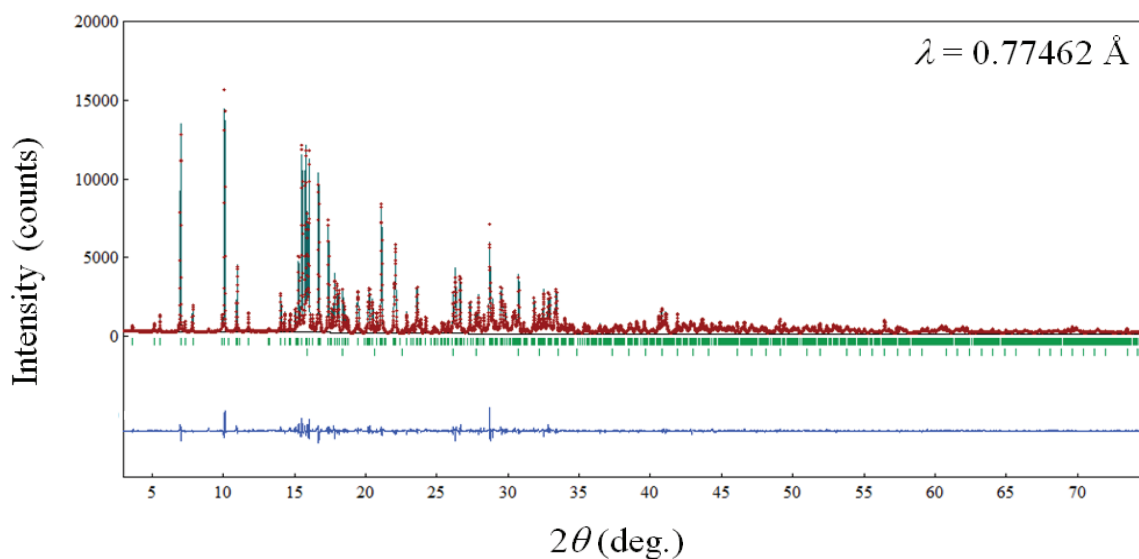


FIGURE 2. The results of Rietveld refinement of CaRhO₃ intermediate phase. Red crosses and the green solid line are observed and calculated XRD patterns, respectively. Black solid line represents refined background curve. At the middle of the panel, upper green bars are calculated peak positions for the intermediate phase, and lower bars are for pyrite-type RhO₂. The blue solid line at the bottom of the illustration shows the difference between observed and calculated patterns. (Color online.)

TABLE 1. Refined structural parameters of CaRhO₃ intermediate phase

Atom	Site	x	y	z	B (Å ²)
O1	2e	0.8215(6)	3/4	0.8756(10)	1.0
O2	2e	0.6152(6)	1/4	0.7842(9)	1.0
O3	2e	0.5488(6)	1/4	0.1325(9)	1.0
O4	2e	0.5535(6)	1/4	0.4159(10)	1.0
O5	2e	0.7031(6)	3/4	0.3271(10)	1.0
O6	2e	0.8115(6)	1/4	0.5802(9)	1.0
O7	2e	0.7878(6)	1/4	0.1278(9)	1.0
O8	2e	0.9118(6)	3/4	0.3879(9)	1.0
O9	2e	0.9890(6)	3/4	0.1170(9)	1.0
Ca1	2e	0.6718(2)	3/4	0.6175(3)	0.88(5)
Ca2	2e	0.6505(2)	3/4	0.9941(3)	0.76(5)
Ca3	2e	0.0521(2)	1/4	0.3318(3)	0.91(5)
Rh1	2e	0.54318(8)	3/4	0.27037(13)	0.34(2)
Rh2	2e	0.89248(9)	1/4	0.99875(12)	0.35(2)
Rh3	2e	0.19426(8)	3/4	0.64612(13)	0.39(2)

Notes: Space group $P2_1/m$ (no. 11). Lattice constants: $a = 12.5114(1)$ Å, $b = 3.1241(1)$ Å, $c = 8.8579(1)$ Å, $\beta = 103.951(1)^\circ$, $V = 336.01(1)$ Å³, $Z = 6$, $V_m = 33.725(1)$ cm³/mol. $R_{wp} = 6.228\%$, $S = 1.5118$. CaRhO₃ intermediate phase $R_B = 0.909\%$, $R_p = 0.476\%$. RhO₂ $R_B = 0.651\%$, $R_p = 0.466\%$.

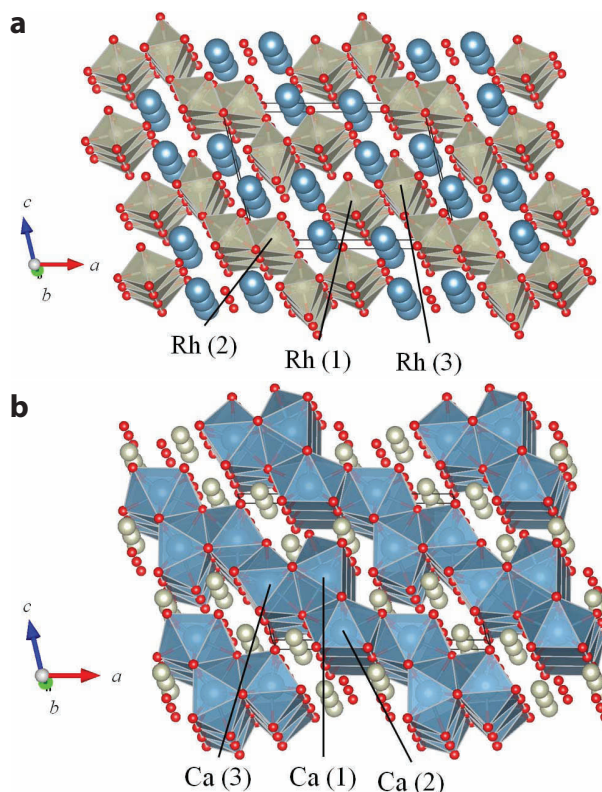
$$R_{wp} \equiv \left\{ \frac{\sum_i w_i [y_i - f_i(x)]^2}{\sum_i w_i y_i^2} \right\}^{1/2}, \quad R_B \equiv \frac{\sum_K |I_K - I_K(x)|}{\sum_K I_K},$$

$$R_F \equiv \frac{\sum_K \left| |F_K| - |F_K(x)| \right|}{\sum_K |F_K|}, \quad \text{and } S \equiv \left\{ \frac{\sum_i w_i [y_i - f_i(x)]^2}{N - P} \right\}^{1/2},$$

where y_i is the observed intensity, $w_i (=1/y_i)$ is the statistical weight based on counting statistics, $f_i(x) [= F(2\theta; x_1, x_2, x_3, \dots)]$ is the calculated intensity at a diffraction angle of 2θ , N is the number of all data points, P is the number of refined parameters, and I_o , $I_c(x)$, F_o and $F_c(x)$ are the observed and calculated integrated intensities and structural factors for reflection K , respectively.

The crystal structure of CaRhO₃ intermediate phase belongs to a new structure type, and Figure 3 illustrates the structure drawn by VESTA (Momma and Izumi 2008). Rh1, Rh2, and Rh3 are sixfold coordinated by oxygen, and Ca1, Ca2, and Ca3 in eight-fold coordination. The coordination numbers of Ca and Rh of the intermediate phase are the same as those of CaRhO₃ perovskite and post-perovskite phases. Selected bond distances are shown in Table 2. (A CIF¹ is on deposit.) The interatomic distances between Rh and O are in the range of 1.92–2.10 Å, which are consistent with the sum of 1.40 Å (^{VI}O²⁻) and 0.60 Å (^{VI}Rh⁴⁺) (effective ionic radii, Shannon 1976). The interatomic distances between Ca and O range from 2.31 to 2.70 Å. Considering the effective ionic radius of ^{VIII}Ca²⁺ (1.12 Å), these lengths are consistent with the sum of the ionic radii. On comparing the interatomic distances of the CaRhO₃ intermediate phase with those of the perovskite and post-perovskite phases reported by Shirako et al. (2009), the average Rh-O distance of the intermediate phase, 1.998 Å, is very close to 1.999 Å of perovskite, and is greater than 1.987 Å of post-perovskite. Also, the average Ca-O distance of the intermediate phase, 2.470 Å, is similar to 2.463 Å of perovskite, and is greater than 2.444 Å of post-perovskite. The effective coordination numbers calculated by VESTA are 5.93 for Rh1, 5.79 for Rh2, 5.97 for Rh3, 7.38 for Ca1, 7.74 for Ca2, and 7.30 for Ca3.

The structure of CaRhO₃ intermediate phase can be compared with those of compounds in the Ca-Rh-O system. In CaRhO₃ intermediate phase, each RhO₆ octahedron shares the edges with the nearest neighbor RhO₆ octahedra to form single RhO₆ octa-

**FIGURE 3.** Crystal structure of CaRhO₃ intermediate phase with (a) RhO₆ octahedra, and with (b) CaO₈ polyhedra. (Color online.)**TABLE 2.** Bond lengths in CaRhO₃ intermediate phase

Bond	Bond length (Å)
Rh1-O2	1.923(7)
Rh1-O3 ×2	1.995(5)
Rh1-O4 ×2	2.010(5)
Rh1-O5	1.942(7)
Rh2-O1 ×2	1.988(5)
Rh2-O7	1.935(8)
Rh2-O9 ⁱ	1.996(6)
Rh2-O9 ⁱⁱ ×2	2.094(5)
Rh3-O5 ×2	2.000(5)
Rh3-O6	1.989(8)
Rh3-O7	1.961(8)
Rh3-O8 ×2	2.025(5)
Ca1-O1	2.584(8)
Ca1-O2 ×2	2.372(6)
Ca1-O4 ×2	2.558(7)
Ca1-O5	2.694(8)
Ca1-O6 ×2	2.426(8)
Ca2-O1	2.600(8)
Ca2-O2 ×2	2.387(6)
Ca2-O3 ⁱⁱⁱ	2.475(7)
Ca2-O3 ^{iv} ×2	2.513(7)
Ca2-O7 ×2	2.411(6)
Ca3-O1	2.697(8)
Ca3-O6 ×2	2.306(6)
Ca3-O8 ^v	2.415(8)
Ca3-O8 ^{vi} ×2	2.488(6)
Ca3-O9 ×2	2.441(6)

Notes: Symmetry codes: (i) $-x, -y, -z$. (ii) x, y, z . (iii) $-x, -y, -z$. (iv) x, y, z . (v) x, y, z . (vi) $-x, -y, -z$.

¹ Deposit item AM-12-002, CIF. Deposit items are available two ways: For a paper copy contact the Business Office of the Mineralogical Society of America (see inside front cover of recent issue) for price information. For an electronic copy visit the MSA web site at <http://www.minsocam.org>, go to the *American Mineralogist* Contents, find the table of contents for the specific volume/issue wanted, and then click on the deposit link there.

hedral chains extending parallel to the **b**-axis (Fig. 3a). Rh₁₀O₆ octahedral chains and Rh₃O₆ octahedral chains share the corners of octahedra to form chains in a similar manner to those in rutile type RhO₂ (Shannon 1968). Two Rh₂O₆ octahedral chains share edges to form double-chain similar to that in calcium-ferrite type CaRh₂O₄ (Yamaura et al. 2005). Combination of four single chains and one double chain of RhO₆ octahedra forms a unit: Rh₁₀O₆-Rh₃O₆-Rh₂O₆-Rh₂O₆-Rh₃O₆-Rh₁₀O₆ sequence. Such RhO₆ octahedral units are not found in the structures of any other known compounds in the system Ca-Rh-O. As shown in Figure 3b, CaO₈ polyhedra form heaved layers. The CaO₈ layers stack up alternatively with the RhO₆ units along the [101] direction. This is similar to post-perovskite type CaRhO₃ (Shirako et al. 2009).

The structure of CaRhO₃ intermediate phase has edge-sharing octahedral chains extending parallel to the **b**-axis. This is different from the type of kinked post-perovskite structures proposed by Oganov et al. (2005) and Tschauner et al. (2008) for MgSiO₃, in which there is extensive corner-sharing between the octahedral chains. Our present findings show another unexpected variation in the structures of the post-perovskite family. To explore possible phases with post-perovskite related structures, it is worth studying high-pressure transitions of perovskites with more various *ABX₃* compositions in detail.

ACKNOWLEDGMENTS

We are grateful to S. Hirai and an anonymous reviewer for their constructive comments. This work was supported in part by Grants-in-Aid for Scientific Research (nos. 19340166 and 22340163 to M.A., nos. 20360012 and 22246083 to K.Y.) from the Japan Society for the Promotion of Science (JSPS), and by Funding Program for World-Leading Innovative R&D on Science and Technology (FIRST Program) managed by JSPS. A.R.O. acknowledges funding from the National Science Foundation (EAR-1114313) and DARPA (grant N66001-10-1-4037), and access to supercomputers at New York Center for Computational Sciences (U.S.A.), Joint Supercomputer Center of the Russian Academy of Sciences (Moscow, Russia), and Moscow State University (Russia). The synchrotron XRD measurement was carried out on the BL02B2 of SPring-8 under the Priority Nanotechnology Support Program administered by the Japan Synchrotron Radiation Research Institute (JASRI) (proposal no. 2010A1669).

REFERENCES CITED

Bloechl, P.E. (1994) Projector augmented-wave method. *Physical Review B*, 50, 17953–17979.

Cheng, J.G., Zhou, J.S., Goodenough, J.B., Sui, Y., Ren, Y., and Suchomel, M.R. (2011) High-pressure synthesis and physical properties of perovskite and post-perovskite Ca_{1-x}Sr_xIrO₃. *Physical Review B*, 83, 064401.

Gao, G., Oganov, A.R., Li, Z., Li, P., Cui, T., Bergara, A., Lyakhov, A.O., Ma, Y., Itaka, T., and Zou, G. (2010) Crystal structures and superconductivity of stannane under high pressure. *Proceedings of National Academy of Sciences*, 107, 1317–1320.

Glass, C.W., Oganov, A.R., and Hansen, N. (2006) USPEX—Evolutionary crystal structure prediction. *Computer Physics Communications*, 175, 713–720.

Hirai, S., Sanehira, T., Nishiyama, N., Irifune, T., Klemme, S., Bromiley, G., and Atffiled, J.P. (2011) Tuning of structure, morphology and magnetism in postperovskite oxide solid solutions. *Chemistry of Materials*, 23, 114–121.

Hirose, K. and Fujita, Y. (2005) Clapeyron slope of the post-perovskite phase transition in CaIrO₃. *Geophysical Research Letters*, 32, L13313, DOI: 10.1029/2005GL023219.

Inaguma, Y., Hasumi, K., Yoshida, M., Ohba, T., and Katsumata, T. (2008) High-pressure synthesis, structure, and characterization of a post-perovskite CaPtO₃ with CaIrO₃-type structure. *Inorganic Chemistry*, 47, 1868–1870.

Izumi, F. and Momma, K. (2007) Three-dimensional visualization in powder diffraction. *Solid State Phenomena*, 130, 15–20.

Kojitani, H., Furukawa, A., and Akaogi, M. (2007a) Thermochemistry and high-pressure equilibria of the post-perovskite phase transition in CaIrO₃. *American Mineralogist*, 92, 229–232.

Kojitani, H., Shirako, Y., and Akaogi, M. (2007b) Post-perovskite phase transition in CaRuO₃. *Physics of the Earth and Planetary Interiors*, 165, 127–134.

Kresse, G. and Furthmüller, J. (1996) Efficient iterative schemes for ab initio total-energy calculations using a plane wave basis set. *Physical Review B*, 54, 11169–11186.

Kresse, G. and Joubert, D. (1999) From ultrasoft pseudopotentials to the projector augmented-wave method. *Physical Review B*, 59, 1758–1775.

Lyakhov, A.O., Oganov, A.R., and Valle, M. (2010) How to predict very large and

complex crystal structures. *Computer Physics Communications*, 181, 1623–1632.

Ma, Y., Erements, M.I., Oganov, A.R., Xie, Y., Trojan, I., Medvedev, S., Lyakhov, A.O., Valle, M., and Prakapenka, V. (2009) Transparent dense sodium. *Nature*, 458, 182–185.

Momma, K. and Izumi, F. (2008) VESTA: a three-dimensional visualization system for electronic and structural analysis. *Journal of Applied Crystallography*, 41, 653–658.

Murakami, M., Hirose, K., Kawamura, K., Sata, N., and Ohishi, Y. (2004) Post-perovskite phase transition in MgSiO₃. *Science*, 304, 855–858.

Oganov, A.R. and Glass, C.W. (2006) Crystal structure prediction using ab initio evolutionary techniques: Principles and applications. *Journal of Chemical Physics*, 124, 244704.

Oganov, A.R. and Ono, S. (2004) Theoretical and experimental evidence for a post-perovskite phase of MgSiO₃ in Earth's D' layer. *Nature*, 430, 445–448.

Oganov, A.R., Martoňák, R., Laio, A., Raiteri, P., and Parrinello, M. (2005) Anisotropy of Earth's D' layer and stacking faults in the MgSiO₃ post-perovskite phase. *Nature*, 438, 1142–1144.

Oganov, A.R., Glass, C.W., and Ono, S. (2006) High-pressure phases of CaCO₃: crystal structure prediction and experiment. *Earth and Planetary Science Letters*, 241, 95–103.

Oganov, A.R., Chen, J., Gatti, C., Ma, Y.-Z., Ma, Y.-M., Glass, C.W., Liu, Z., Yu, T., Kurakevich, O.O., and Solozhenko, V.L. (2009) Ionic high-pressure form of elemental boron. *Nature*, 457, 863–867.

Oganov, A.R., Ma, Y.M., Xu, Y., Errea, I., Bergara, A., and Lyakhov, A.O. (2010a) Exotic behavior and crystal structures of calcium under pressure. *Proceedings of National Academy of Sciences*, 107, 7646–7651.

Oganov, A.R., Ma, Y., Lyakhov, A.O., Valle, M., and Gatti, C. (2010b) Evolutionary crystal structure prediction as a method for the discovery of minerals and materials. In R. Wentzcovitch and L. Stixrude, Eds., *Theoretical and Computational Methods in Mineral Physics*, 71, p. 271–298. *Reviews in Mineralogy and Geochemistry*, Mineralogical Society of America, Chantilly, Virginia.

Oganov, A.R., Lyakhov, A.O., and Valle, M. (2011) How evolutionary crystal structure prediction works, and why. *Accounts for Chemical Research*, 44, 227–237.

Ogushi, K., Gotou, H., Yagi, T., Kiuchi, Y., Sakai, F., and Ueda, Y. (2006) Metal-insulator transition in Ca_{1-x}Na_xIrO₃ with post-perovskite structure. *Physical Review B*, 74, 241104.

Ogushi, K., Matsushita, Y., Miyajima, N., Katsuya, Y., Tanaka, M., Izumi, F., Gotou, H., Ueda, Y., and Yagi, T. (2008) CaPtO₃ as a novel post-perovskite oxide. *Physics and Chemistry of Minerals*, 35, 189–195.

Perdew, J.P., Burke, K., and Ernzerhof, M. (1996) Generalized gradient approximation made simple. *Physical Review Letters*, 77, 3865–3868.

Shannon, R.D. (1968) Synthesis and properties of two new members of the rutile family RhO₂ and PtO₂. *Solid State Communications*, 6, 139–143.

——— (1976) Revised effective ionic radii and systematic studies of interatomic distances in halides and chalcogenides. *Acta Crystallographica*, A32, 751–767.

Shirako, Y., Kojitani, H., Akaogi, M., Yamaura, K., and Takayama-Muromachi, E. (2009) High-pressure phase transitions of CaRhO₃ perovskite. *Physics and Chemistry of Minerals*, 36, 455–462.

Shirako, Y., Satsukawa, H., Kojitani, H., Katsumata, T., Yoshida, M., Inaguma, Y., Hiraki, K., Takahashi, T., Yamaura, K., Takayama-Muromachi, E., and Akaogi, M. (2010) Magnetic properties of high-pressure phase of CaRuO₃ with post-perovskite structure. *Journal of Physics: Conference Series*, 215, 012038, DOI: 10.1088/1742-6596/215/1/012038.

Shirako, Y., Satsukawa, H., Wang, X.X., Li, J.J., Guo, Y.F., Arai, M., Yamaura, K., Yoshida, M., Kojitani, H., Katsumata, T., Inaguma, Y., Hiraki, K., Takahashi, T., and Akaogi, M. (2011) Integer spin-chain antiferromagnetism of the 4d post-perovskite oxide CaRuO₃. *Physical Review B*, 83, 174411.

Tateno, S., Hirose, K., Sata, N., and Ohishi, Y. (2010) Structural distortion of CaSnO₃ perovskite under pressure and the quenchable post-perovskite phase as a low pressure analogue to MgSiO₃. *Physics of the Earth and Planetary Interiors*, 181, 54–59.

Tschauner, O., Kiefer, B., Liu, H., Sinogeikin, S., Somayazulu, M., and Luo, S.N. (2008) Possible structural polymorphism in Al-bearing magnesium silicate post-perovskite. *American Mineralogist*, 93, 533–539.

Yamanaka, T., Mao, W.L., Mao, H.K., Hemley, R.J., and Shen, G. (2010) New structure and spin state of iron-rich (Mg,Fe)SiO₃ post-perovskite. *Journal of Physics: Conference Series*, 215, 012100, DOI: 10.1088/1742-6596/215/1/012100.

Yamaura, K. and Takayama-Muromachi, E. (2006) High-pressure synthesis of the perovskite rhodate CaRhO₃. *Physica C*, 445–448, 54–56.

Yamaura, K., Huang, Q., Moldovan, M., Young, D.P., Sato, A., Baba, Y., Nagai, T., Matsui, Y., and Takayama-Muromachi, E. (2005) High-pressure synthesis, crystal structure determination, and a Ca substitution study of the metallic rhodium oxide NaRh₂O₄. *Chemistry of Materials*, 17, 359–365.

Yamaura, K., Shirako, Y., Kojitani, H., Arai, M., Young, D.P., Akaogi, M., Nakashima, M., Katsumata, T., Inaguma, Y., and Takayama-Muromachi, E. (2009) Synthesis and magnetic and charge transport properties of the correlated 4d post-perovskite CaRhO₃. *Journal of American Chemical Society*, 131, 2722–2726.

MANUSCRIPT RECEIVED APRIL 6, 2011

MANUSCRIPT ACCEPTED SEPTEMBER 18, 2011

MANUSCRIPT HANDLED BY WENDY MAO